Nanoscale Advances

PAPER

View Article Online
View Journal | View Issue

Cite this: *Nanoscale Adv.*, 2019, **1**, 322

Construction of *in situ* self-assembled $FeWO_4$/g-C_3N_4 nanosheet heterostructured Z-scheme photocatalysts for enhanced photocatalytic degradation of rhodamine B and tetracycline†

Ramakrishna Dadigala, [a] RajKumar Bandi, [a] Bhagavanth Reddy Gangapuram[ab] and Veerabhadram Guttena *[a]

Although photocatalytic degradation is an ideal strategy for cleaning environmental pollution, it remains challenging to construct a highly efficient photocatalytic system by steering the charge flow in a precise manner. In this work, a novel, highly efficient, stable, and visible light active hybrid photocatalytic system consisting of $FeWO_4$ and g-C_3N_4 nanosheets (CNNs) has been successfully prepared by an *in situ* self-assembly solvothermal approach. Several characterization techniques were employed to study the phase structures, morphologies, optical properties, surface composition and chemical state of the as-prepared samples. SEM and TEM results demonstrated that the $FeWO_4$ nanoparticles are uniformly dispersed on the surface of CNNs with a diameter of about 10–20 nm, which could provide maximum interfacial contact and a synergistic coupling effect between $FeWO_4$ and CNNs. XPS and FTIR results confirmed that there was strong electrostatic interaction between $FeWO_4$ and CNNs, suggesting the formation of heterojunctions between them. In addition, UV-DRS and PL spectroscopy revealed that the $FeWO_4$/CNN composites exhibited increased visible light absorption and improved charge generation/separation efficiency. As a result, the photocatalytic activity of the $FeWO_4$/CNNs was enhanced in comparison with pure $FeWO_4$ and CNNs for rhodamine B (RhB) and tetracycline (TC) degradation under natural sunlight irradiation. The photocatalytic efficiency of the optimal $FeWO_4$/CNN composite (10 wt% $FeWO_4$/CNNs) for the degradation of RhB (TC) was about 13.26 (4.95) and 86.2 (31.1) times higher than that of pure $FeWO_4$ and CNNs, respectively. Meanwhile, the 10 wt% $FeWO_4$/CNN sample exhibits good photocatalytic stability in recycling experiments. The enhanced photocatalytic activity may be attributed to the formation of the Z-scheme system between $FeWO_4$ and CNNs, effectively prolonging the lifetime of the photoexcited electrons generated by CNNs and the photoexcited holes generated by $FeWO_4$, which was subsequently confirmed by the active species trapping experiments and the calculation of relative band alignments. This work opens up a new feasible avenue to synthesize visible light active Z-scheme photocatalysts for application in energy production and environmental remediation.

Received 15th June 2018
Accepted 3rd September 2018

DOI: 10.1039/c8na00041g

rsc.li/nanoscale-advances

1. Introduction

Over the past few decades, environmental pollution has become one of the greatest problems to society. The effluents produced by many industries, such as textile, pharmaceutical, cosmetic, leather, and food industries, are identified as the primary source of water contamination, which is harmful to the environment, and hazardous to human health as well as ecosystems.[1–3] Due to their stable chemical structures and recalcitrance to biological degradation, conventional wastewater treatment processes are not always efficient in the removal of these pollutants.[4–6] As a result, they have been frequently detected in a variety of environmental matrices, including surface, ground and potable water, soils and even the food on our table. There is therefore a need for the development of efficient treatment technologies for the removal of these compounds from wastewater. A "green" photocatalytic strategy that utilizes solar energy has been considered as a sustainable solution to solve the above-mentioned problems.[7–12] Nevertheless, the photocatalytic performance of most semiconductor photocatalysts available is located at a low level, and their

[a]*Department of Chemistry, Osmania University, Hyderabad, Telangana State, 500007, India*

[b]*Department of Chemistry, PG Center Wanaparthy, Palamuru University, Mahabub Nagar, Telangana State, 509001, India. E-mail: gvbhadram@gmail.com*

† Electronic supplementary information (ESI) available: A part of the Experimental section, time-dependent UV-vis absorption spectra of rhodamine B and tetracycline solution, and XRD patterns and FTIR spectra of the 10-FWO/CNN composite before and after photocatalytic reaction. See DOI: 10.1039/c8na00041g

practical application is hampered by some internal effects, such as poor visible light utilization, lower photogenerated electron–hole pair separation, and the lack of active species generation.[13–15] Thus, to maximize the utilization of solar light, the development of visible light active photocatalysts with sufficient charge separation ability and high photocatalytic stability is still an arduous task in photocatalysis research. Hence, the fabrication of heterojunctions is an effective and attractive strategy to restrain the recombination rate of photogenerated charge carriers.[16–18] Nevertheless, it is difficult to simultaneously achieve high charge separation efficiency and strong redox ability. Recently, the construction of artificial Z-scheme photocatalytic systems has emerged as an alternative method, because it can not only separate the photogenerated electron–hole pairs but also maintain the excellent redox capacity of the constituent semiconductors.[19–21] However, the majority of the synthesized artificial Z-scheme photocatalytic systems usually had mediators (*e.g.* redox pairs (Fe^{3+}/Fe^{2+} and IO_3^-/I^-))[22,23] and noble metals (Ag and Au),[24,25] which will bring about great difficulties in their practical application.[19] Thus, developing a mediator-free direct Z-scheme photocatalytic system as an ideal and effective method has become a hotspot for application in environmental purification and hydrogen generation from water.[26–31]

Recently, two-dimensional (2D) materials have been widely studied in photocatalysis due to their unique structural and optical properties, of which the g-C_3N_4 material gained special attention because it is abundant, sustainable, environmentally friendly and has a suitable band gap and high chemical stability, making it potentially suitable for solar energy conversion and environmental purification.[32–36] Unfortunately, pure g-C_3N_4 seriously suffers from poor photocatalytic efficiency because of a high recombination rate of photogenerated charge carriers.[37–40] Besides, it is reported that g-C_3N_4 nanosheets show considerably superior photocatalytic activity compared to the bulk g-C_3N_4 resulting from the reduction of internal defects and improvement of the specific surface area.[41,42] It can be predicted that the photocatalytic activity of g-C_3N_4-based photocatalysts may be further enhanced by increasing the specific surface area of bulk g-C_3N_4. Thus, it is accepted that the construction of g-C_3N_4-based Z-scheme photocatalysts with a narrow band gap semiconductor may provide bright prospects for dealing with the increasingly serious environmental pollution.

Recent studies have investigated some metal tungstates as potential co-catalyst candidates for photocatalytic applications, which could effectively reduce the recombination of charge carriers for improving the degradation of pollutants.[43–45] Among these tungstates, the investigation of iron tungstate ($FeWO_4$) has been widely reported in the literature due to its narrow band gap, and good magnetic and photocatalytic properties.[46,47] Recently, $FeWO_4$ has been explored for photocatalytic reactions with no co-catalysts.[48,49] Furthermore, suitable matching of the band levels of $FeWO_4$ with g-C_3N_4 nanosheets to form a direct Z-scheme photocatalytic system offers appropriate driving forces to separate and transfer photogenerated electron–hole pairs. As $FeWO_4$ and g-C_3N_4 are both visible light driven photocatalysts, after combining the $FeWO_4$ photocatalyst with g-C_3N_4 nanosheets, the obtained $FeWO_4$/g-C_3N_4 nanosheet composite may be a promising candidate for efficient photocatalytic activity under visible light irradiation. However, to the best of our knowledge, no group has reported *in situ* growth of $FeWO_4$ nanoparticles on the surface of g-C_3N_4 nanosheets by a facile solvothermal method for the degradation of RhB and TC under sunlight irradiation.

Based on the above considerations, herein we grew $FeWO_4$ nanoparticles on the surface of g-C_3N_4 nanosheets by a facile solvothermal method to form composite catalysts for efficient degradation of organic pollutants and these composites were found to exhibit superior photocatalytic activity compared with the pure $FeWO_4$, g-C_3N_4 nanosheets and mechanically mixed catalyst. It was found that the composite photocatalysts exhibited not only an improved photocatalytic activity but also excellent stability and reusability during the photocatalytic process, which can be mainly attributed to the synergistic effect between $FeWO_4$ and g-C_3N_4 nanosheets. Furthermore, a possible direct Z-scheme mechanism for the enhanced photocatalytic activity of the $FeWO_4$/g-C_3N_4 nanosheet composite was also discussed based on the relative band gap positions of these two semiconductors and the free radical trapping experimental results. Detailed characterization of the structure, composition, and optical properties of the as-prepared photocatalysts was also carried out.

2. Experimental section

2.1. Preparation of bulk g-C_3N_4 and g-C_3N_4 nanosheets

Bulk g-C_3N_4 (CN) was prepared by thermal polymerization of melamine at high temperature in a muffle furnace.[50] In detail, 5 g of melamine was placed in a crucible with a cover, and then, it was heated at 600 °C for 2 h with a ramp rate of about 3 °C min^{-1}. After cooling to room temperature, the obtained yellow agglomerates were collected and ground into fine powder. After that, g-C_3N_4 nanosheets (CNNs) were prepared by using the liquid exfoliation method.[50] In detail, 100 mg of the as-prepared CN was dispersed in 100 mL of double distilled water, then the mixture was sonicated for 16 h and then the resulting suspension was centrifuged at 5000 rpm to remove the residual un-exfoliated g-C_3N_4. Then, the final suspension was dried at 80 °C overnight.

2.2. Preparation of $FeWO_4$/g-C_3N_4 nanosheet composites

$FeWO_4$/CNN composites were synthesized through a solvothermal method.[47,51] First, an appropriate amount of the as-prepared CNNs was dispersed in 36 mL of ethylene glycol by sonication for 30 min, to facilitate the uniform growth of $FeWO_4$ nanoparticles on their surface. Then, 5 mmol of $FeCl_3 \cdot 6H_2O$ dissolved in 2 mL double distilled water was added to the CNN suspension and stirred magnetically for 30 min. Subsequently, 5 mmol of $Na_2WO_4 \cdot 2H_2O$ dissolved in 2 mL of double distilled water was added dropwise to the above mixture. 10 mmol of sodium acetate was then added to the above mixture with continuous stirring. After 30 min of stirring, the above suspension was transferred into a Teflon-lined stainless steel

autoclave (50 mL) and reacted at 200 °C for 12 h. After cooling down to room temperature naturally, the products obtained were collected by centrifugation, washed several times with double distilled water and ethanol, and dried in an oven at 80 °C for 12 h. The as-prepared $FeWO_4$/CNN composites with various $FeWO_4$ amounts of 5, 10, 15 and 20 wt% were denoted as 5-FWO/CNNs, 10-FWO/CNNs, 15-FWO/CNNs and 20-FWO/CNNs, respectively. Pure $FeWO_4$ nanoparticles were also synthesized under the same conditions without adding any CNN powder.

In addition, a control sample was also prepared by mechanical grinding of CNNs and $FeWO_4$. A mixture of $FeWO_4$ and CNNs was finely ground and then calcined at 200 °C for 12 h. After cooling to room temperature, the resultant product was collected and crushed to powder for further use. The mass ratio of $FeWO_4$ and CNNs in the sample was the same as that in the optimal composite catalyst of $FeWO_4$/CNNs [10-FWO/CNNs]. The control sample was denoted as $FeWO_4$ + CNNs. More details about the materials and characterization methods are provided in the ESI.†

2.3. Measurement of photocatalytic activity

The photocatalytic activities of the as-prepared photocatalysts were evaluated by the degradation of rhodamine B (RhB) and tetracycline (TC) under natural sunlight irradiation. All of the photocatalytic experiments were carried out during the same time on sunny days and the sunlight intensity was found to be around 100 000 lx to 110 000 lx. In a typical experiment, 50 mg of photocatalyst was suspended in an aqueous solution of RhB (50 mL, 10 mg L^{-1}) and TC (50 mL, 20 mg L^{-1}), and then the suspensions were stirred in the dark for 1 h to reach the adsorption–desorption equilibrium between the photocatalyst and model pollutants, after which the reaction suspension was irradiated for 90 min. At certain time intervals, 4 mL aliquots were sampled and centrifuged to remove the photocatalyst, and the concentrations of the remnant RhB and TC were analyzed by recording the absorbance using an UV-Vis spectrophotometer (UV-2600, Shimadzu). A blank test was also carried out without any photocatalyst under sunlight irradiation to evaluate the efficiency of the photocatalyst. Furthermore, the reusability of 10-FWO/CNNs was tested by four consecutive cycles for the degradation of RhB. After each cycle, the catalyst was separated from the reaction mixture by centrifugation and washed with double distilled water and dried overnight in an oven at 80 °C for use in the next cycle.

2.4. Analysis of reactive species

To investigate the active species generated during the photodegradation process, ammonium oxalate (AO, 1 mM), isopropanol (IPA, 1 mM), and 1,4-benzoquinone (BQ, 1 mM) were used as the hole (h^+), hydroxyl radical ($^{\bullet}OH$), and superoxide radical ($^{\bullet}O_2^-$) scavengers,[50] respectively. The method was similar to the above photocatalytic activity test. The $^{\bullet}OH$ content was also measured by the PL technique, using terephthalic acid (TA) as a probe molecule.[52]

3. Results and discussion

A facile *in situ* solvothermal method was designed for the preparation of $FeWO_4$/g-C_3N_4 nanosheet photocatalysts, and the preparation process is illustrated in Scheme 1. Firstly, the g-C_3N_4 nanosheets obtained from the bulk g-C_3N_4 through a liquid exfoliation method were dispersed in ethylene glycol by sonication. Then, upon addition of $FeCl_3$ solution to the above reaction mixture, the Fe^{3+} ions were reduced to Fe^{2+} ions because of the reducing ability of ethylene glycol. Then, with the addition of $NaWO_4$ solution and sodium acetate (here sodium acetate provided an alkaline environment), the Fe^{2+} ions reacted with WO_4^{2-} ions to generate $FeWO_4$ nuclei on the g-C_3N_4 nanosheet surface under constant stirring. As the solvothermal treatment time increased, the $FeWO_4$ nuclei grew into nanoparticles through a self-assembly growth mechanism.[47] In this case, g-C_3N_4 nanosheets not only act as the support to form heterostructures but are also employed as dispersants to hinder the aggregation of $FeWO_4$ nanoparticles. Finally, $FeWO_4$/CNN heterostructured photocatalysts were obtained.

3.1. Characterization of photocatalysts

The crystalline phases of the as-prepared samples were examined by XRD analysis. Fig. 1a shows the XRD patterns of the CN, CNNs, $FeWO_4$ and $FeWO_4$/CNN composites. The pure CN has two significant peaks at 27.4° and 13.1°, indexed to the (002)

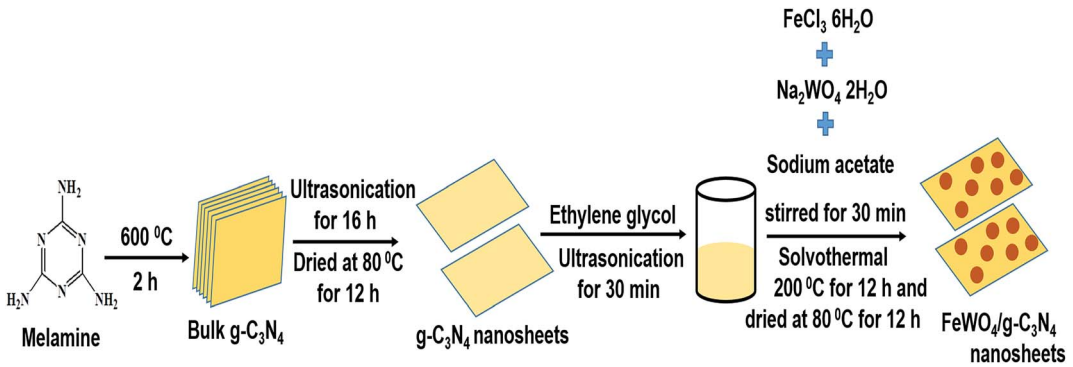

Scheme 1 Schematic representation of the preparation of bulk g-C_3N_4, g-C_3N_4 nanosheets and $FeWO_4$/g-C_3N_4 nanosheet composites.

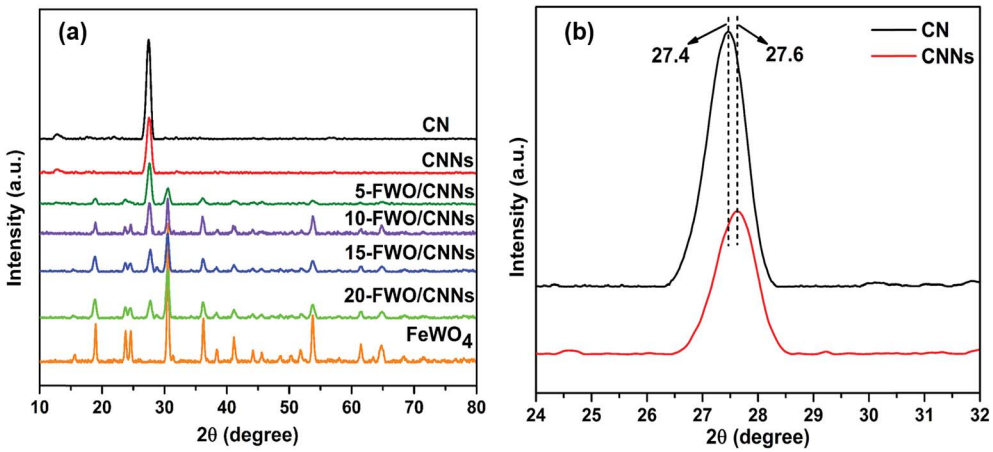

Fig. 1 (a) XRD patterns of CN, CNNs, $FeWO_4$ and the $FeWO_4$/CNNs composites and (b) magnified curves of CN and CNNs.

and (100) diffraction planes of g-C_3N_4, corresponding to the characteristic inter-layer stacking of aromatic systems and the in-plane structural packing motif of tri-*s*-triazine units,[53–55] respectively. Interestingly, in the case of CNNs, the intensity of diffraction peaks significantly decreased, indicating that the CNN structure has been successfully obtained after exfoliation.[56] Besides, the dominant (002) peak in CNNs shifted slightly to a higher angle (Fig. 1b), which may be due to the decreased distance between the layers and which is in good agreement with previous reports.[57] For pure $FeWO_4$, the positions of all peaks can be well indexed to the monoclinic phase of $FeWO_4$ (JCPDS card no. 46-1446).[51] It can also be found that the diffraction peaks of $FeWO_4$/CNN composites consisted of the characteristic peaks of $FeWO_4$ and CNNs, which implied the coexistence of $FeWO_4$ and CNN phases in the as-prepared $FeWO_4$/CNN composites. As the $FeWO_4$ concentration increases from 5 to 20 wt%, the diffraction peaks of $FeWO_4$ gradually intensify, whereas the peaks of CNNs are weakened and no phase structural changes have been detected, suggesting that the introduction of $FeWO_4$ did not change the phase structure of g-C_3N_4 during the *in situ* growth process. The above results confirm that the $FeWO_4$/CNN composites are successfully constructed.

The morphology and microstructure of the as-prepared samples were investigated by SEM and TEM. Fig. 2a–d show the SEM images of CN, CNNs, $FeWO_4$ and the 10-FWO/CNNs composite, respectively. As shown in Fig. 2a, the pure CN has a layered structure composed of tightly stacked g-C_3N_4 nanosheets several micrometers in size. And as expected, after exfoliation, the CNNs (Fig. 2b) exhibited a clear two-dimensional

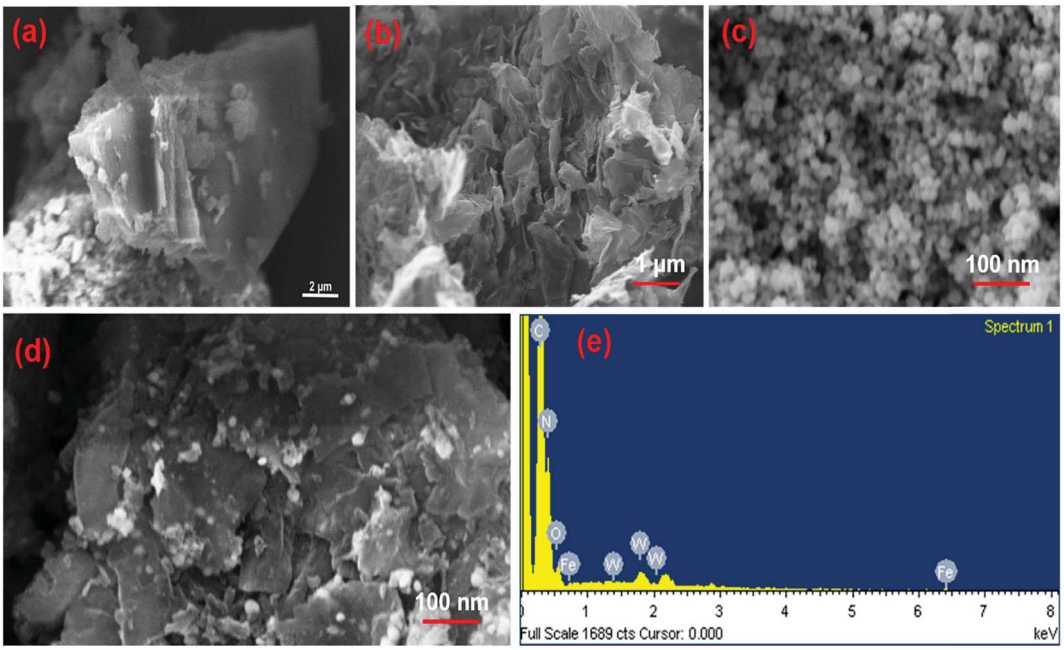

Fig. 2 SEM images of (a) CN, (b) CNNs, (c) $FeWO_4$ and (d) the 10-FWO/CNNs composite; and (e) the corresponding EDS image of the 10-FWO/CNN composite.

sheet-like structure with wrinkled edges, which further confirmed the successful exfoliation of CN.[50] Furthermore, the thickness of CNNs decreases dramatically, which may result in an increase in the specific surface area and reactive species.[57] From Fig. 2c, it can be seen that pure $FeWO_4$ exhibited spherical shapes with a diameter of 10–20 nm. In the case of the 10-FWO/CNN composite (Fig. 2d), we can clearly see that numerous $FeWO_4$ nanoparticles are well dispersed on the surface of CNNs. The EDS spectrum analysis of the 10-FWO/CNN composite (Fig. 2e) reveals that it contains of C, N, Fe, W, and O elements, which further confirmed the coexistence of CNN and $FeWO_4$ phases in the $FeWO_4$/CNN composites.

TEM was also performed to further confirm the morphology of CNNs and the $FeWO_4$/CNN composite formed. The TEM image shown in Fig. 3a further proved that the CNNs have a lamellar structure, with several stacking layers. The TEM image of 10-FWO/CNNs in Fig. 3b demonstrates that the $FeWO_4$ nanoparticles are uniformly dispersed on the surface of CNNs with a diameter of about 10–20 nm, which is in good agreement with the SEM results. Given the different morphologies of $FeWO_4$ and CNNs, the dark parts in the TEM image should be $FeWO_4$, while the light parts correspond to CNNs. These highly dispersed $FeWO_4$ nanoparticles could provide maximum interfacial contact with the CNN surface, which could further strengthen the synergistic coupling effect between $FeWO_4$ and CNNs. Moreover, the intimate contact between $FeWO_4$ and CNNs would further strengthen the photogenerated charge separation and transfer.[58] To observe in detail the interface between $FeWO_4$ and CNNs, HRTEM analysis was also performed. As shown in Fig. 3a and c, a lattice spacing of 0.326 nm that corresponds to the (002) crystallographic plane of g-C_3N_4 (ref. 38 and 59) and a clear lattice fringe of 0.37 nm ascribed to the (002) planes of $FeWO_4$ (ref. 51) were observed, which confirms the formation of heterojunctions *via* the *in situ* growth of $FeWO_4$ on the CNN surface. The formed interface is favorable for the transport of photogenerated charge carriers, and thereby promotes the separation of electron–hole pairs.

XPS analysis was performed to investigate the surface chemical states and bonding configuration of the pure CNNs and 10-FWO/CNN composite and the results (survey and high resolution spectra) are shown in Fig. 4. The survey XPS spectrum (Fig. 4a) of the 10-FWO/CNN composite exhibited strong C 1s and N 1s peaks related to the g-C_3N_4 phase, together with Fe 2p, W 4f and O 1s peaks related to the $FeWO_4$ phase without any contamination, and the survey XPS spectrum of CNNs contains C 1s, N 1s and O 1s peaks. In addition, the small peak of O 1s in CNNs is assigned to adsorbed oxygen species. Fig. 4b shows the high-resolution spectra of C 1s. Pure CNNs show two peaks at 284.6 eV and 288.1 eV, which can be assigned to the sp^2 C–C bond and sp^2 bonded carbon of N–C=N coordination present in the triazine rings of g-C_3N_4, respectively.[43] The 10-FWO/CNN composite also displayed the two C 1s peaks. However, compared with pure CNNs, the binding energy of 10-FWO/CNNs at 288.1 eV was shifted to 288.4 eV, while the position of the peak at 284.6 remained unchanged. The N 1s spectrum of CNNs (Fig. 4c) was deconvoluted into three peaks at 398.8, 399.8 and 401.1 eV, which could be assigned to sp^2 hybridized aromatic nitrogen atoms bonded to carbon atoms (C–N=C), tertiary nitrogen groups (N–$(C)_3$), and uncondensed amino groups (C–N–H), respectively.[43] The N 1s binding energies of CNNs shifted to 339.1, 400.4 and 401.5 eV for 10-FWO/CNNs, respectively. These results indicate that the carbon and nitrogen

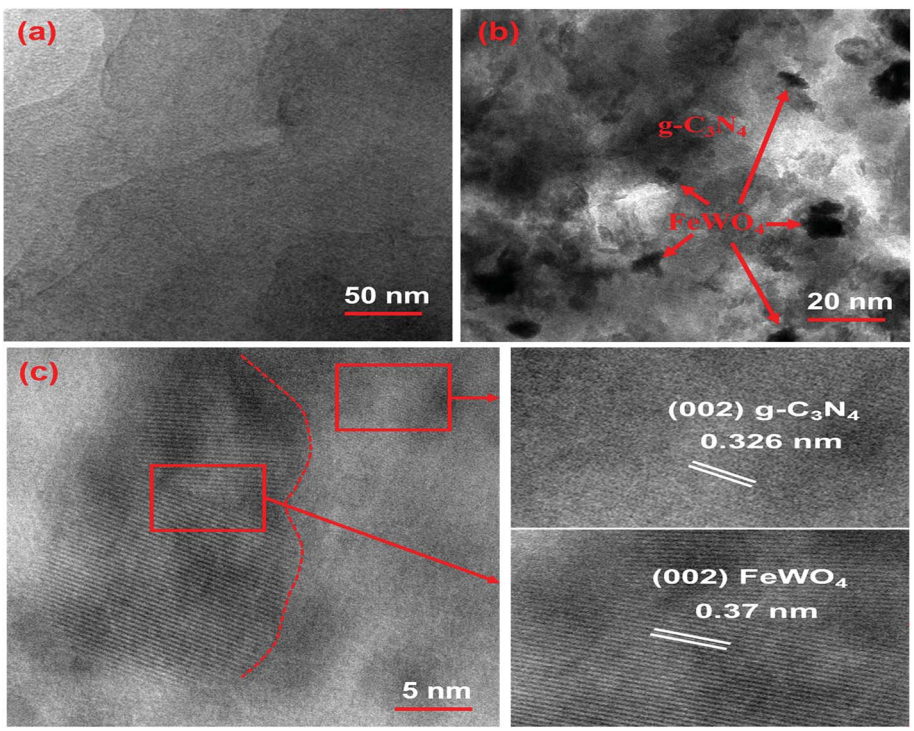

Fig. 3 TEM images of the (a) CNNs and (b) 10-FWO/CNN composite; and (c) HRTEM image of the 10-FWO/CNN composite.

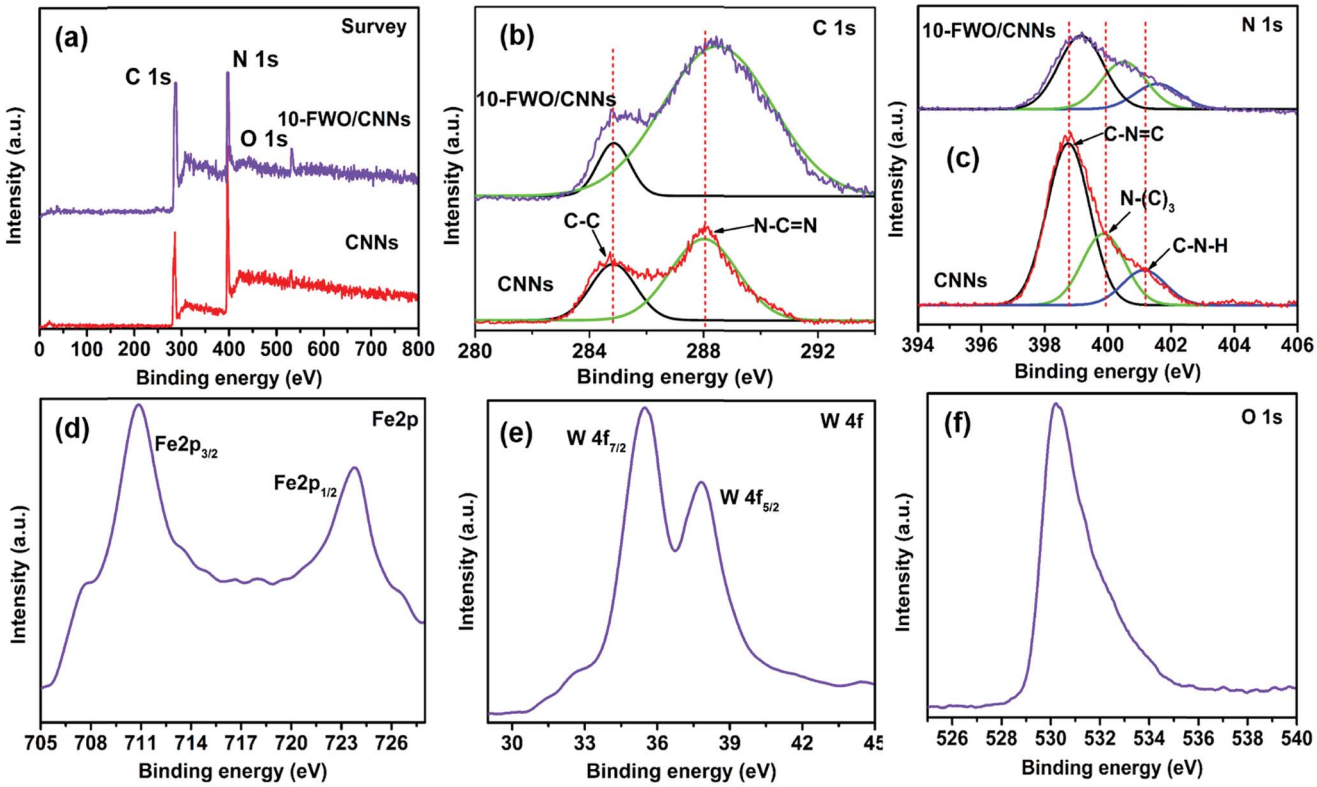

Fig. 4 (a) XPS survey spectra of the CNNs and 10-FWO/CNN composite; high-resolution XPS spectra of (b) C 1s and (c) N 1s for CNNs and the 10-FWO/CNN composite; and high-resolution XPS spectra of (d) Fe 2p, (e) W 4f and (f) O 1s for the 10-FWO/CNN composite.

atoms present in CNNs formed the binding interaction with metal species of $FeWO_4$. In Fig. 4d, the peaks at 710.4 and 723.9 eV are assigned to the binding energies of Fe $2p_{3/2}$ and $2p_{1/2}$ respectively, and are characteristic of Fe^{2+} in the $FeWO_4$ material.[51] The W 4f peaks at 35.5 and 37.8 eV in Fig. 4e correspond to the W $4f_{7/2}$ and W $4f_{5/2}$ binding energies of W^{6+} in $FeWO_4$,[60] respectively. The O 1s peak at 530.1 eV (Fig. 4f) corresponds to the $FeWO_4$ oxygen atom.[60] The shifting of C 1s and N 1s peaks and presence of Fe 2p, W 4f and O 1s peaks in the 10-FWO/CNN composite can be ascribed to the fact that $FeWO_4$ hybridized with CNNs during the *in situ* growth process, also indicating that certain chemical interactions are possibly formed between them, as observed in TEM images.

The chemical structure and functional groups of the as-prepared samples were studied using FTIR spectra and the results are shown in Fig. 5a. For the FTIR spectrum of pure $FeWO_4$, the absorption bands appearing at 834 and 877 cm^{-1} were due to the symmetrical vibrations of bridging oxygen atoms of Fe–O–W. The absorption band at 650–680 cm^{-1} can be due to the stretching mode of W–O in WO_6 octahedra and the absorption band at 556 cm^{-1} is the characteristic stretching vibration of the Fe–O bond in hematite particles.[43] In the FTIR spectrum of CN, the series of bands observed in the region of 1200–1650 cm^{-1} are ascribed to the stretching vibration of C–N heterocycles, while the broad band at 3000–3500 cm^{-1} is ascribed to the stretching vibration of N–H groups and surface adsorbed hydroxyl groups. In addition, the band at 810 cm^{-1} originates from a breathing mode of *s*-triazine units.[28,54,61] It can be seen that the characteristic FTIR spectrum of CNNs is similar to that of CN, indicating that the g-C_3N_4 chemical structure has not been destroyed after the exfoliation process. Moreover, the FTIR spectra of the $FeWO_4$/CNNs composites are similar to that of pure CNNs, and all the characteristic absorption bands of CNNs appear in the composites, suggesting that no structural change of CNNs occurs during the composite formation. After introducing $FeWO_4$ into CNNs, the characteristic bands from the C–N heterocycles of CNNs appear as blue shifts (Fig. 5b), indicating that there might be some interactions between the C–N heterocycles of g-C_3N_4 and $FeWO_4$. From the TEM, XPS and FTIR results, we concluded that there was strong electrostatic interaction between $FeWO_4$ and CNNs, which could promote photogenerated electron–hole pair separation and transfer, and further enhance the photocatalytic performance of the $FeWO_4$/CNN composites.

The light absorption properties of the as-prepared samples were examined by UV-vis DRS analysis (Fig. 6). As shown in Fig. 6a, CNNs show a slight blue shift of the absorption edge with respect to that of CN, which is ascribed to the quantum confinement effect of g-C_3N_4 nanosheets and is consistent with previous reports.[62] The pure $FeWO_4$ exhibited profound absorption over a wide spectral region from UV to visible light. After the introduction of $FeWO_4$ into CNNs, the composite samples exhibited stronger optical absorption in the visible region compared with CNNs, and the absorption intensities of these composites are strengthened with an increase in the $FeWO_4$ content. This demonstrates well that the *in situ* grown $FeWO_4$ nanoparticles can act as a sensitizer for enhancing the

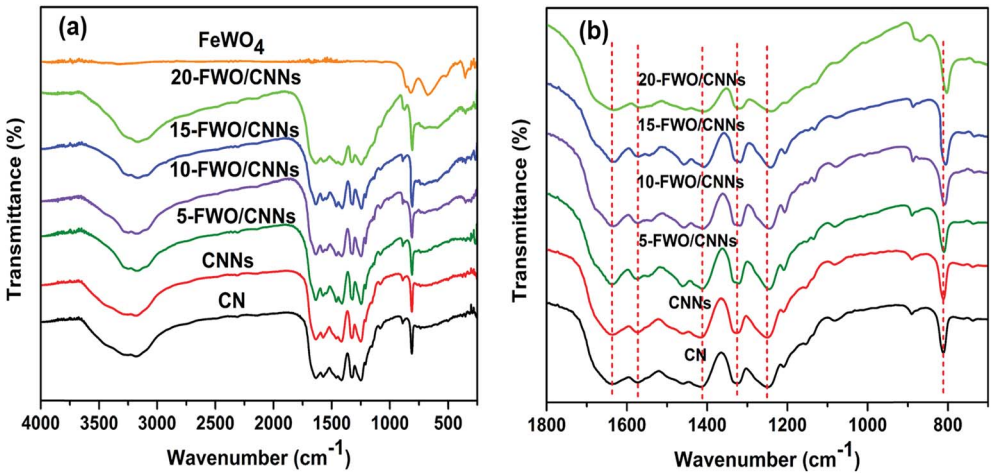

Fig. 5 (a) FTIR spectra of CN, CNNs, $FeWO_4$ and the $FeWO_4$/CNN composites; and (b) magnified curves in the range of 700 to 1800 cm^{-1}.

visible light absorption of CNNs, suggesting that the $FeWO_4$/CNN composites can harvest more light energy and produce more photogenerated charge carriers.

The energy level and band gap of the semiconductors play a crucial role in determining their physical properties. The band gap energies of the as-prepared photocatalysts can be calculated using the following formula[45]

$$\alpha h\nu = A(h\nu - E_g)^{n/2}$$

where α, h, ν, A and E_g represent the absorption coefficient, Planck's constant, light frequency, proportionality constant related to the material, and energy band gap, respectively. The band gap energy for $FeWO_4$ was determined from a plot of $(\alpha h\nu)^2$ *versus* $h\nu$ ($n = 1$ for direct transition)[63] and that for the CNNs was obtained from a plot of $(\alpha h\nu)^{1/2}$ *versus* $h\nu$ ($n = 4$ for indirect transition).[64] As shown in Fig. 6b and c, the band gap energies of CN, CNNs and $FeWO_4$ are estimated to be around 2.7, 2.73 and 2.1 eV, respectively.

Generally, the PL spectra of photocatalysts can be used to illustrate the recombination rate of the photogenerated electron–hole pairs; it is known that higher PL intensity usually means more recombination of electron–hole pairs and lower photocatalytic activity. Fig. 7 shows the PL spectra of the as-

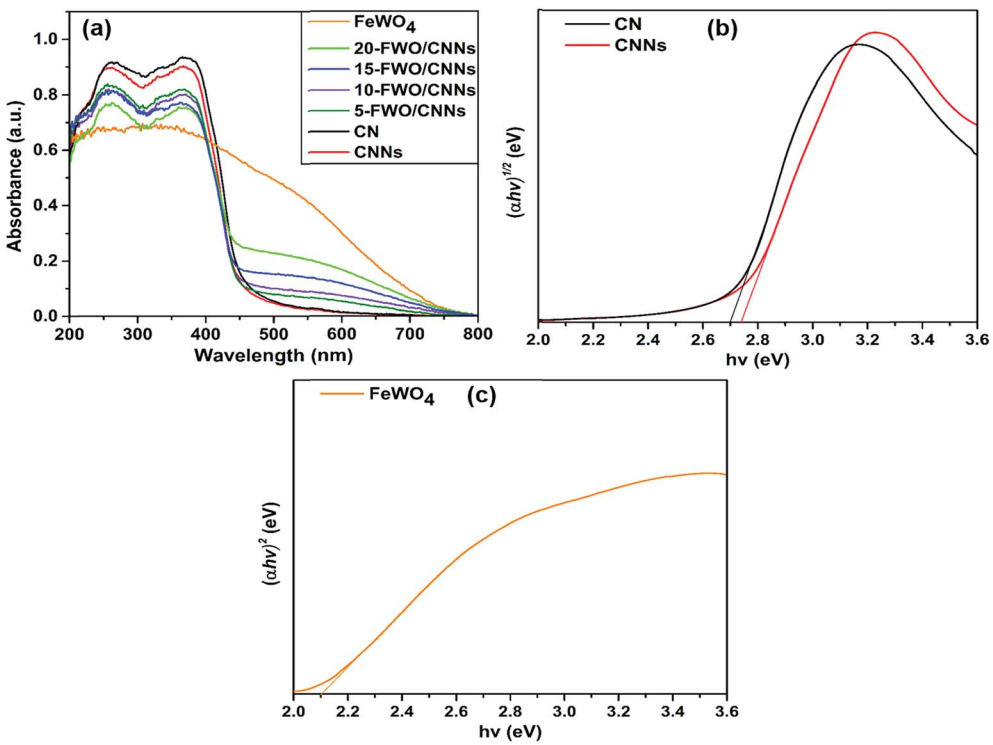

Fig. 6 (a) UV-vis diffuse reflectance spectra of CN, CNNs, $FeWO_4$ and the $FeWO_4$/CNN composites; (b) $(\alpha h\nu)^{1/2}$ *versus* $h\nu$ plot of CNNs and CN; and (c) $(\alpha h\nu)^2$ *versus* $h\nu$ plot of $FeWO_4$.

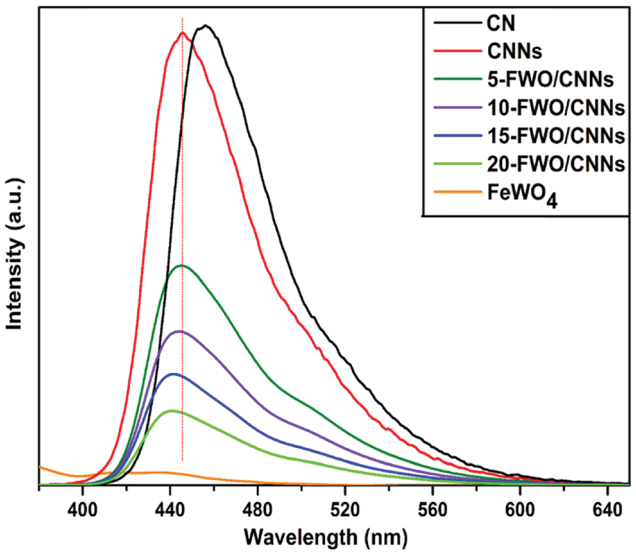

Fig. 7 PL spectra of CN, CNNs, $FeWO_4$ and the $FeWO_4$/CNN composites.

prepared samples. It can be observed that both the CN and CNNs have a strong PL peak at an excitation wavelength of 360 nm, which could be related to the recombination of the photogenerated electron–hole pairs in g-C_3N_4. A blue shifted peak for CNNs compared with that for CN is mainly due to shifted conduction band and valence band edges, which is caused by the well-known quantum confinement effect.[62] After coupling CNNs with $FeWO_4$, the emission peak intensities decreased significantly, indicating that the recombination of electron–hole pairs is greatly suppressed by the introduction of $FeWO_4$. One reason might be that coupling with $FeWO_4$ may change the transition path of photogenerated electrons to the ground state for CNNs, which may result from interactions between CNNs and $FeWO_4$. As a result, the charge separation could be promoted on the $FeWO_4$/CNN composites, leading to the higher photocatalytic activity of the composite photocatalysts. From Fig. 7, it can also be seen that the PL peak positions shifted to lower wavelengths with the increase in the amount of $FeWO_4$. This may be caused by the strong interaction between the $FeWO_4$ and CNNs in the composite samples, which also occurred in the g-C_3N_4–WO_3 system.[59]

3.2. Photocatalytic performance

In order to investigate the photocatalytic activities of the as-prepared samples, RhB and TC were chosen as model pollutants for photocatalytic degradation (Fig. 8). Negligible self-degradation was observed for RhB and TC under sunlight irradiation for ~90 min (Fig. 8a and b). As expected, all $FeWO_4$/CNN composites exhibited higher photocatalytic activities than pure $FeWO_4$, CN and CNNs with a hierarchical order of 10-FWO/CNNs > 5-FWO/CNNs > 15-FWO/CNNs > 20-FWO/CNNs,

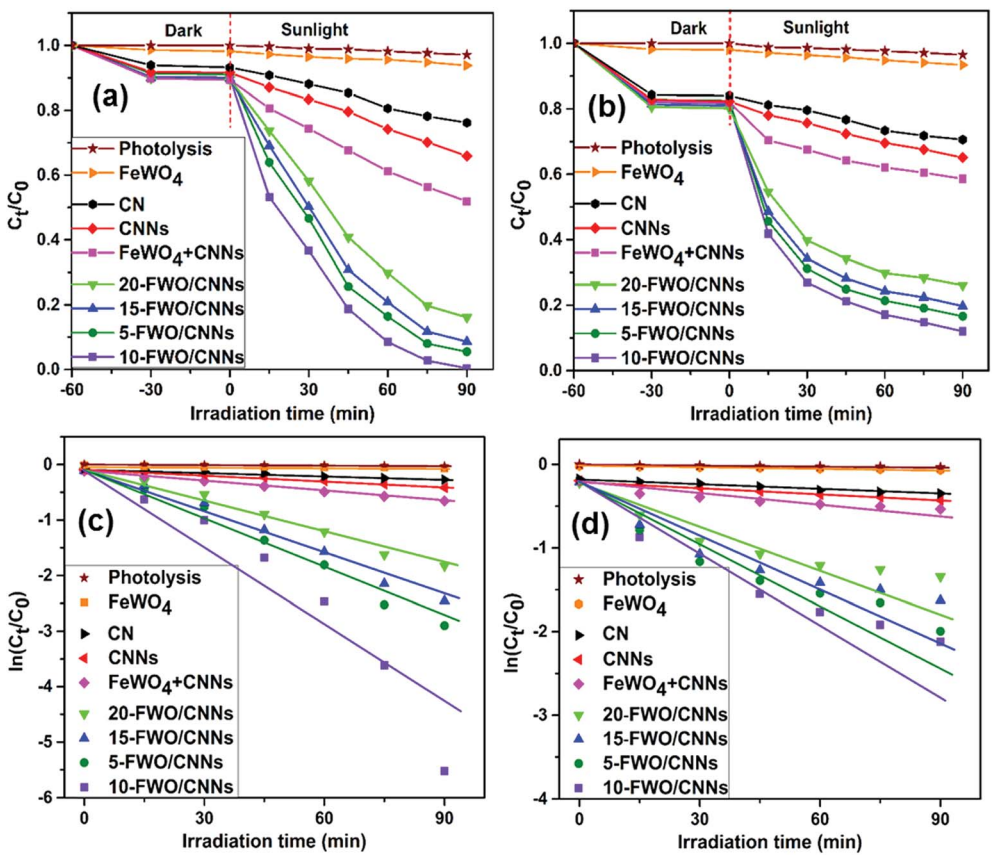

Fig. 8 Photocatalytic degradation rate of (a) RhB, and (b) TC over CN, CNNs, $FeWO_4$ and the $FeWO_4$/CNN composites; the pseudo-first-order kinetics fitted curves of (c) RhB, and (d) TC over CN, CNNs, $FeWO_4$ and the $FeWO_4$/CNN composites under sunlight irradiation.

indicating that the $FeWO_4$ content influenced the photocatalytic activity of the as-prepared composites notably. This could be explained by the effective separation of photogenerated electron–hole pairs due to the formation of heterojunctions between $FeWO_4$ and CNNs in the composites. Moreover, the activities of the composite samples were found to increase with the increase in the $FeWO_4$ content from 5 wt% (94.5% for RhB, 83.4% for TC) to 10 wt% (99.6% for RhB, 88% for TC), and then decrease with further increase in the $FeWO_4$ content from 10 wt% to 20 wt% (83.9% for RhB, 73.9% for TC), suggesting that the $FeWO_4$/CNN composites had the highest photocatalytic activity with the optimum $FeWO_4$ content of 10 wt%. The reason for this may be that when the amount of $FeWO_4$ is lower than its optimum amount, the trapping sites of carriers increase with the increase of the $FeWO_4$ amount, which prolongs the lifetime of carriers, thus improving the photocatalytic activity. However, when the amount of $FeWO_4$ is higher than its optimum amount, excessive $FeWO_4$ (15 wt% and 20 wt%) may be clustered and effective heterojunction photocatalysts are not formed. Furthermore, the excessive deposition of $FeWO_4$ may increase the light opacity, preventing CNNs from absorbing light effectively, which leads to a decrease in the photocatalytic activity. Therefore, CNNs coated with an appropriate amount of $FeWO_4$ form an effective heterojunction photocatalyst, so that the photocatalytic performance will be maximum.

A physical mixture of $FeWO_4$ and CNNs (defined as $FeWO_4$ + CNNs) was also tested for RhB and TC degradation, and it exhibited much weaker photocatalytic activity as compared to the *in situ* synthesized $FeWO_4$/CNN composites. This fact indicates that intimate contact between $FeWO_4$ and CNNs is crucial for the interfacial charge transfer between the two semiconductors, which improves the separation efficiency of photogenerated electron–hole pairs and ultimately enhances the photocatalytic activity.

To quantitatively study the reaction kinetics of RhB and TC degradation, the experimental data were analyzed using the pseudo-first-order kinetic model, $\ln(C_t/C_0) = -kt$,[52] where k is the rate constant, C_0 is the initial concentration of RhB or TC, and C_t is the concentration of RhB or TC at time t. This equation is well built for photocatalytic experiments when the pollutant is in the millimolar concentration range. The k value can be determined by a linear fit of the plot of $\ln(C_t/C_0)$ *versus* reaction time, as shown in Fig. 8c and d. The calculated k values for RhB and TC degradation over all the photocatalysts are listed in Table 1; it can be seen that the k values of 10-FWO/CNNs for RhB and TC photodegradation were 86.2 times and 31.1 times higher than that of pure $FeWO_4$, and 13.26 and 4.95 times as high as that of individual CNNs, respectively, revealing that the introduction of $FeWO_4$ greatly influences the performance of the composite photocatalysts. As a result, the 10-FWO/CNNs were the optimal performing sample among all composites.

The time-dependent UV-vis absorption spectral changes of the RhB and TC under sunlight irradiation in the presence of 10-FWO/CNNs are shown in Fig. S1a and b.† The characteristic peak intensities of RhB and TC gradually decreased by prolonging the irradiation time, revealing the degradation of the pollutants. The shifts of the characteristic peaks indicate the presence of decomposition products of the pollutants.

Table 1 The calculated reaction rate constants (min^{-1}) for $FeWO_4$, CN, CNNs, $FeWO_4$ + CNNs, 5-FWO/CNNs, 10-FWO/CNNs, 15-FWO/CNNs and 20-FWO/CNNs toward photodegradation of RhB and TC

	Rate constant (min^{-1})	
Photocatalyst	Rhodamine B	Tetracycline
$FeWO_4$	0.000711	0.000757
CN	0.00302	0.00368
CNNs	0.00463	0.00476
$FeWO_4$ + CNNs	0.00728	0.00593
5-FWO/CNNs	0.0322	0.0222
10-FWO/CNNs	0.0614	0.0236
15-FWO/CNNs	0.0272	0.0181
20-FWO/CNNs	0.0203	0.0150

In addition to the photocatalytic activity, the stability of photocatalysts is another important parameter for practical application. To evaluate the stability and reusability of the $FeWO_4$/CNN composites, recycling reactions were performed for the photodegradation of RhB over the optimized catalyst (10-FWO/CNNs) under sunlight irradiation (Fig. 9). As shown in Fig. 9, very interestingly, no significant reduction of photocatalytic efficiency was observed up to the fourth cycle (there was a slight decrease derived from the loss of the photocatalyst during the cycling process), which implies the high stability of the photocatalyst during photodegradation. The XRD and FTIR patterns of the 10-FWO/CNN composite were also investigated after four recycling runs. As shown in Fig. S2a and b,† the XRD and FTIR patterns of the 10-FWO/CNN composite before and after reaction reveal that the phase and structure remained unchanged. Therefore, it is evident that the $FeWO_4$/CNN composite does not undergo any photocorrosion or photobleaching during the degradation experiments.

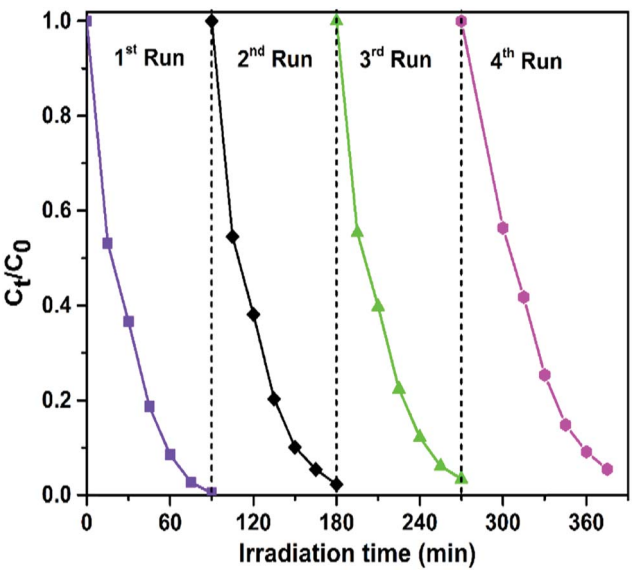

Fig. 9 Recycling photocatalytic tests of the 10-FWO/CNN composite for RhB degradation.

3.3. Photocatalytic mechanism

To investigate the photocatalytic degradation mechanism of the $FeWO_4$/CNN composites, a series of sacrificial agents were used to quench the relevant active species during the photocatalytic process, and the results are shown in Fig. 10a. As shown in Fig. 10a, when AO was added to the reaction system, the photocatalytic efficiency was not obviously changed. Therefore, it seems that holes are not the reactive species. However, when BQ and IPA were added to the reaction system, the photocatalytic efficiencies were reduced from 99.6% to 14.1 and 19.3% for RhB, respectively. Based on the results, it is suggested that $^{\bullet}O_2^-$ and $^{\bullet}OH$ are the major reactive species in the photocatalytic reaction system. To further confirm the presence of $^{\bullet}OH$ in the $FeWO_4$/CNN system during sunlight irradiation, $^{\bullet}OH$ trapping PL experiments using terephthalic acid (TA) as a probe molecule were also carried out (Fig. 10b). As shown in Fig. 10b, after 30 min of irradiation, a strong PL signal is observed at 425 nm and the intensity significantly increased with the irradiation time as compared to dark treatment, which indeed indicates the generation of $^{\bullet}OH$ radicals.

For the sake of theoretical investigation of the mechanism of photodegradation, the valence band (VB) and conduction band (CB) edge potentials of the $FeWO_4$ and g-C_3N_4 were determined using the following empirical equations:[45]

$$E_{VB} = \chi - E^e + 0.5E_g$$

$$E_{CB} = E_{VB} - E_g$$

where E_{VB} and E_{CB} are the valence and conduction band edge potentials, respectively; χ is the absolute electronegativity of the semiconductor, which is the geometric mean of the electronegativity of the constituent atoms; E^e is the energy of free electrons on the hydrogen scale (about 4.5 eV *vs.* NHE); and E_g is the bandgap energy of the semiconductor (the E_g values for $FeWO_4$ and CNNs are 2.10 eV and 2.73 eV, respectively). The χ values for $FeWO_4$ and g-C_3N_4 are calculated to be 6.3 eV (ref. 60) and 4.73 eV,[45] respectively. Accordingly, the VB values of semiconductors $FeWO_4$ and CNNs are calculated to be 2.85 and 1.595 eV, and the CB values of semiconductors $FeWO_4$ and CNNs are calculated to be 0.75 and −1.135 eV, respectively.

In theory, the photogenerated electrons in the CB of $FeWO_4$ cannot reduce O_2 to give $^{\bullet}O_2^-$, because the CB edge potential of $FeWO_4$ (0.75 eV *vs.* NHE) is more positive than the standard redox potentials of $O_2/^{\bullet}O_2^-$ (−0.33 eV *vs.* NHE).[27,45] However, the photogenerated holes in the VB of $FeWO_4$ can oxidize H_2O to give $^{\bullet}OH$, because the VB potential of $FeWO_4$ is more positive than the standard redox potentials of $H_2O/^{\bullet}OH$ (2.68 eV *vs.* NHE).[26,58] For the CNNs, because the CB edge potential of CNNs (−1.135 eV *vs.* NHE) is more negative than the standard redox potentials of $O_2/^{\bullet}O_2^-$, the photogenerated electrons can reduce O_2 to give $^{\bullet}O_2^-$. Meanwhile, since the VB potential of CNNs is lower than the standard redox potentials of $H_2O/^{\bullet}OH$, the photogenerated holes in the VB of CNNs cannot oxidize H_2O to give $^{\bullet}OH$.

If the charge carrier transfer in the $FeWO_4$/CNN composites occurs through a type-II heterojunction mechanism (Fig. 11a), the electrons in the CB of CNNs will migrate to the CB of $FeWO_4$, and the holes in the VB of $FeWO_4$ will migrate to the VB of CNNs. As a result, the electrons get accumulated in the CB of $FeWO_4$ and cannot reduce O_2 to $^{\bullet}O_2^-$, and the holes get accumulated in the VB of CNNs and cannot oxidize H_2O to $^{\bullet}OH$. Hence, this kind of electron–hole transfer process is not favorable for the formation of active species, and leads to lower photocatalytic activity of the reaction system. Nevertheless, the radical trapping experiment and TAPL analysis implied that $^{\bullet}O_2^-$ and $^{\bullet}OH$ are the major reactive species in the $FeWO_4$/CNN photocatalytic system, and the photocatalyst exhibited higher photocatalytic activity. Therefore the separation process of the photogenerated electron–hole pairs in this system did not follow the type-II heterojunction mechanism, but might have occurred through the Z-scheme mechanism.

On the basis of the above experimental results and band structure analysis of $FeWO_4$ and CNNs, a Z-scheme mechanism was proposed to explain the enhanced photocatalytic performance of the $FeWO_4$/CNN composites and is schematically illustrated in Fig. 11b. Under illumination of sunlight, both $FeWO_4$ and CNNs can be excited to generate electron–hole pairs. The photogenerated electrons in the CB of $FeWO_4$ tend to transfer and recombine with the photogenerated holes in the VB of CNNs. In this way, the larger number of photogenerated

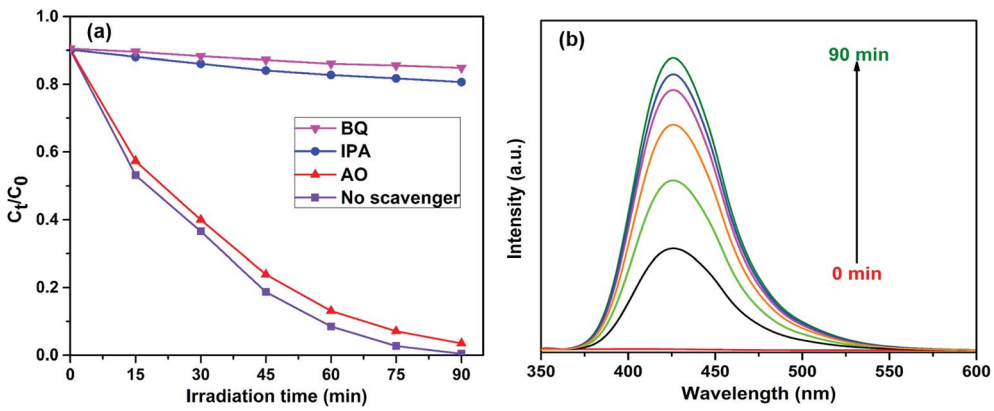

Fig. 10 (a) Effect of different scavengers on degradation of RhB in the presence of the 10-FWO/CNN composite; and (b) $^{\bullet}OH$ trapping PL spectra of the 10-FWO/CNN composite with TA solution under sunlight irradiation.

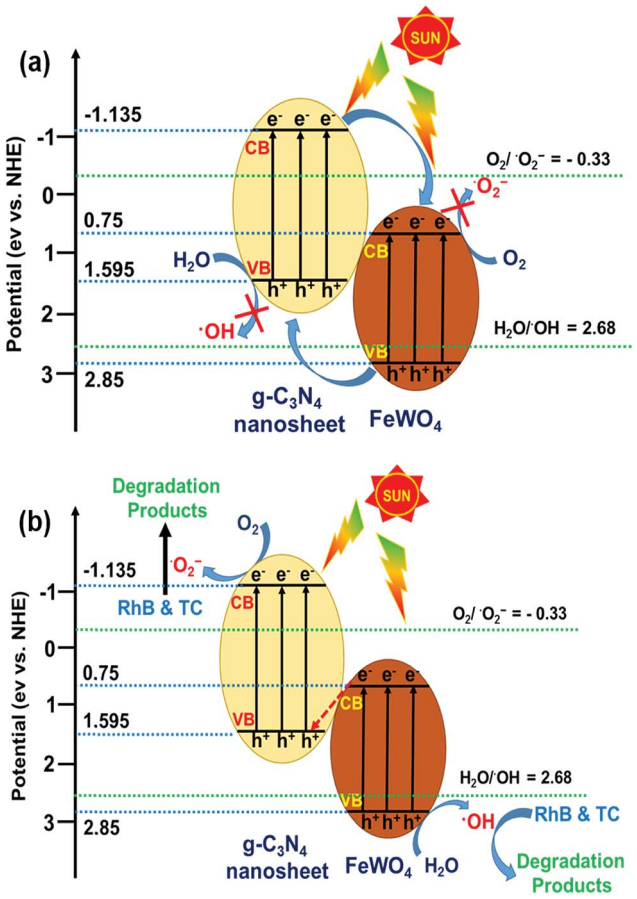

Fig. 11 (a) Schematic diagram for the impossible generation of reactive species in the $FeWO_4$/CNN composites; and (b) schematic diagram for the charge transfer in the direct Z-scheme $FeWO_4$/CNN composites.

electrons accumulated in the CB of CNNs can reduce the adsorbed O_2 to form more $^{\bullet}O_2^-$. Meanwhile, the photogenerated holes left behind in the VB of $FeWO_4$ can oxidize the adsorbed H_2O to give $^{\bullet}OH$. Therefore, the photocatalytic activity of the $FeWO_4$/CNN system is significantly increased, and RhB or TC is decomposed by $^{\bullet}O_2^-$ and $^{\bullet}OH$ reactive species. Therefore, a conclusion can be drawn that the photocatalytic reaction of the as-prepared $FeWO_4$/CNN composites followed a direct Z-scheme mechanism, which could improve the photogenerated electron–hole pair separation and transfer and show a strong oxidation and reduction ability for the effective degradation of organic pollutants.

4. Conclusions

In summary, a series of $FeWO_4$/CNN composites with various contents of $FeWO_4$ have been successfully synthesized through *in situ* growth of self-assembled $FeWO_4$ nanoparticles on the surface of CNNs *via* a facile solvothermal method. The as-prepared $FeWO_4$/CNN composites exhibited excellent photocatalytic activity compared to the pure $FeWO_4$, CN, CNNs and mechanically mixed catalyst in the degradation of RhB and TC under sunlight irradiation. This enhancement could be attributed to the high separation and easy transfer of photogenerated electron–hole pairs in the hybrid system, which can be reasonably attributed to the suitable matching of conduction and valence band levels between $FeWO_4$ and CNNs. Besides, a novel Z-scheme photocatalytic mechanism in the $FeWO_4$/CNN system was confirmed by active species trapping experiments and band energy potentials. Moreover, the $FeWO_4$/CNN composites are very stable and reusable during the photocatalytic reactions. Therefore, the novel $FeWO_4$/CNN photocatalysts may have potential for application in pollutant removal as well as water splitting in the future. This work opens up a new feasible avenue to synthesize visible light active Z-scheme photocatalysts for application in energy production and environmental remediation.

Conflicts of interest

There are no conflicts of interest to declare.

Acknowledgements

One of the authors (Ramakrishna Dadigala) gratefully acknowledges UGC-INDIA for a Senior Research Fellowship. The authors would like to thank the Materials Research Centre, MNIT, Jaipur, India for providing analytical facilities. The authors are also thankful to DST-FIST, New Delhi, India and the Department of Chemistry, Osmania University (OU) and CFRD-OU for providing infrastructure and other necessary facilities.

References

1 L. Yosefi and M. Haghighi, *Appl. Catal., B*, 2018, **220**, 367–378.
2 S. Bagheri, A. TermehYousefi and T.-O. Do, *Catal. Sci. Technol.*, 2017, **7**, 4548–4569.
3 A. Helal, F. A. Harraz, A. A. Ismail, T. M. Sami and I. A. Ibrahim, *Appl. Catal., B*, 2017, **213**, 18–27.
4 Q. Zheng, D. P. Durkin, J. E. Elenewski, Y. Sun, N. A. Banek, L. Hua, H. Chen, M. J. Wagner, W. Zhang and D. Shuai, *Environ. Sci. Technol.*, 2016, **50**, 12938–12948.
5 X. Qu, P. J. J. Alvarez and Q. Li, *Water Res.*, 2013, **47**, 3931–3946.
6 M. Yan, Y. Wu, Y. Yan, X. Yan, F. Zhu, Y. Hua and W. Shi, *ACS Sustainable Chem. Eng.*, 2016, **4**, 757–766.
7 M. N. Chong, B. Jin, C. W. K. Chow and C. Saint, *Water Res.*, 2010, **44**, 2997–3027.
8 F. Opoku, K. K. Govender, C. G. C. E. van Sittert and P. P. Govender, *Adv. Sustainable Syst.*, 2017, **1**, 1700006.
9 A. Kubacka, M. Fernández-García and G. Colón, *Chem. Rev.*, 2012, **112**, 1555–1614.
10 H. Kisch, *Angew. Chem., Int. Ed.*, 2012, **51**, 2–38.
11 N. Serpone and A. V. Emeline, *J. Phys. Chem. Lett.*, 2012, **3**, 673–677.
12 C. Chen, W. Ma and J. Zhao, *Chem. Soc. Rev.*, 2010, **39**, 4206–4219.

13 F. Le Formal, S. R. Pendlebury, M. Cornuz, S. D. Tilley, M. Grätzel and J. R. Durrant, *J. Am. Chem. Soc.*, 2014, **136**, 2564–2574.
14 R. Li, F. Zhang, D. Wang, J. Yang, M. Li, J. Zhu, X. Zhou, H. Han and C. Li, *Nat. Commun.*, 2013, **4**, 1432.
15 F. Huang, D. Chen, X. L. Zhang, R. A. Caruso and Y. Cheng, *Adv. Funct. Mater.*, 2010, **20**, 1301–1305.
16 J. Low, J. Yu, M. Jaroniec, S. Wageh and A. A. Al-Ghamdi, *Adv. Mater.*, 2017, **29**, 1601694.
17 H. Wang, L. Zhang, Z. Chen, J. Hu, S. Li, Z. Wang, J. Liu and X. Wang, *Chem. Soc. Rev.*, 2014, **43**, 5234–5244.
18 Y. Wang, Q. Wang, X. Zhan, F. Wang, M. Safdar and J. He, *Nanoscale*, 2013, **5**, 8326–8339.
19 P. Zhou, J. Yu and M. Jaroniec, *Adv. Mater.*, 2014, **26**, 4920–4935.
20 K. Maeda, *ACS Catal.*, 2013, **3**, 1486–1503.
21 L. Jiang, X. Yuan, G. Zeng, J. Liang, Z. Wu and H. Wang, *Environ. Sci.: Nano*, 2018, **5**, 599–615.
22 K. Maeda, D. Lu and K. Domen, *ACS Catal.*, 2013, **3**, 1026–1033.
23 Y. Sasaki, A. Iwase, H. Kato and A. Kudo, *J. Catal.*, 2008, **259**, 133–137.
24 J. Li, H. Yuan and Z. Zhu, *RSC Adv.*, 2016, **6**, 70563–70572.
25 J.-M. Li, H.-Y. Cheng, Y.-H. Chiu and Y.-J. Hsu, *Nanoscale*, 2016, **8**, 15720–15729.
26 L. Zou, H. Wang and X. Wang, *ACS Sustainable Chem. Eng.*, 2017, **5**, 303–309.
27 H. Xu, L. Liu, X. She, Z. Mo, Y. Xu, L. Huang, Y. Song and H. Li, *RSC Adv.*, 2016, **6**, 80193–80200.
28 P. Xia, B. Zhu, B. Cheng, J. Yu and J. Xu, *ACS Sustainable Chem. Eng.*, 2018, **6**, 965–973.
29 R. He, J. Zhou, H. Fu, S. Zhang and C. Jiang, *Appl. Surf. Sci.*, 2018, **430**, 273–282.
30 J. Li, M. Zhang, Q. Li and J. Yang, *Appl. Surf. Sci.*, 2017, **391**, 184–193.
31 D. Xu, B. Cheng, W. Wang, C. Jiang and J. Yu, *Appl. Catal., B*, 2018, **231**, 368–380.
32 W. J. Ong, L. L. Tan, Y. H. Ng, S. T. Yong and S. P. Chai, *Chem. Rev.*, 2016, **116**, 7159–7329.
33 Y. Zheng, L. Lin, B. Wang and X. Wang, *Angew. Chem., Int. Ed.*, 2015, **54**, 12868–12884.
34 X. Wang, S. Blechert and M. Antonietti, *ACS Catal.*, 2012, **2**, 1596–1606.
35 Y. Cui, Z. Ding, X. Fu and X. Wang, *Angew. Chem., Int. Ed.*, 2012, **51**, 11814–11818.
36 J. Zhang, G. Zhang, X. Chen, S. Lin, L. Möhlmann, G. Dołęga, G. Lipner, M. Antonietti, S. Blechert and X. Wang, *Angew. Chem., Int. Ed.*, 2012, **51**, 3183–3187.
37 D. A. Giannakoudakis, Y. Hu, M. Florent and T. J. Bandosz, *Nanoscale Horiz.*, 2017, **2**, 356–364.
38 X. Zhou, C. Shao, S. Yang, X. Li, X. Guo, X. Wang, X. Li and Y. Liu, *ACS Sustainable Chem. Eng.*, 2018, **6**, 2316–2323.
39 J. Zhang, M. Zhang, R. Q. Sun and X. Wang, *Angew. Chem., Int. Ed.*, 2012, **51**, 10145–10149.
40 G. Zhang, M. Zhang, X. Ye, X. Qiu, S. Lin and X. Wang, *Adv. Mater.*, 2014, **26**, 805–809.
41 X. Dong and F. Cheng, *J. Mater. Chem. A*, 2015, **3**, 23642–23652.
42 Y. Li, L. Fang, R. Jin, Y. Yang, X. Fang, Y. Xing and S. Song, *Nanoscale*, 2015, **7**, 758–764.
43 K. Buvaneswari, R. Karthiga, B. Kavitha, M. Rajarajan and A. Suganthi, *Appl. Surf. Sci.*, 2015, **356**, 333–340.
44 L. Sun, X. Zhao, C. Jia, Y. Zhou, X. Cheng, P. Li, L. Liu and W. Fan, *J. Mater. Chem.*, 2012, **22**, 23428–23438.
45 K. Huang, Y. Hong, X. Yan, C. Huang, J. Chen, M. Chen, W. Shi and C. Liu, *CrystEngComm*, 2016, **18**, 6453–6463.
46 X. Cao, Y. Chen, S. Jiao, Z. Fang, M. Xu, X. Liu, L. Li, G. Pang and S. Feng, *Nanoscale*, 2014, **6**, 12366–12370.
47 Y. Zhou, H. Yao, Q. Zhang, J. Gong, S. Liu and S. Yu, *Inorg. Chem.*, 2009, **48**, 1082–1090.
48 J. Guo, X. Zhou, Y. Lu, X. Zhang, S. Kuang and W. Hou, *J. Solid State Chem.*, 2012, **196**, 550–556.
49 Z. Chen, H. Ma, J. Xia, J. Zeng, J. Di, S. Yin, L. Xu and H. Li, *Ceram. Interfaces*, 2016, **42**, 8997–9003.
50 R. Dadigala, R. Bandi, B. R. Gangapuram and V. Guttena, *J. Photochem. Photobiol., A*, 2017, **342**, 42–52.
51 Y. Ma, Y. Guo, H. Jiang, D. Qu, J. Liu, W. Kang, Y. Yi, W. Zhang, J. Shi and Z. Han, *New J. Chem.*, 2015, **39**, 5612–5620.
52 R. Dadigala, B. R. Gangapuram, R. Bandi, A. Dasari and V. Guttena, *Acta Metall. Sin.*, 2016, **29**, 17–27.
53 S. Patnaik, G. Swain and K. M. Parida, *Nanoscale*, 2018, **10**, 5950–5964.
54 Z. Mao, J. Chen, Y. Yang, D. Wang, L. Bie and B. D. Fahlman, *ACS Appl. Mater. Interfaces*, 2017, **9**, 12427–12435.
55 Z. Lin and X. Wang, *Angew. Chem., Int. Ed.*, 2013, **52**, 1735–1738.
56 N. Cheng, J. Tian, Q. Liu, C. Ge, A. H. Qusti, A. M. Asiri, A. O. Al-Youbi and X. Sun, *ACS Appl. Mater. Interfaces*, 2013, **5**, 6815–6819.
57 Y. Li, K. Li, Y. Yang, L. Li, Y. Xing, S. Song, R. Jin and M. Li, *Chem.–Eur. J.*, 2015, **21**, 17739–17747.
58 S. Zhang, H. Gao, X. Liu, Y. Huang, X. Xu, N. S. Alharbi, T. Hayat and J. Li, *ACS Appl. Mater. Interfaces*, 2016, **8**, 35138–35149.
59 S. Chen, Y. Hu, X. Jiang, S. Meng and X. Fu, *Mater. Chem. Phys.*, 2015, **150**, 512–521.
60 F. Wang, W. Li, S. Gu, H. Li, X. Liu and M. Wang, *ACS Sustainable Chem. Eng.*, 2016, **4**, 6288–6298.
61 J. Sun, J. Zhang, M. Zhang, M. Antonietti, X. Fu and X. Wang, *Nat. Commun.*, 2012, **3**, 1137–1139.
62 X. Zhang, X. Xie, H. Wang, J. Zhang, B. Pan and Y. Xie, *J. Am. Chem. Soc.*, 2013, **135**, 18–21.
63 J. Zhang, Y. Wang, S. Li, X. Wang, F. Huang, A. Xie and Y. Shen, *CrystEngComm*, 2011, **13**, 5744–5750.
64 S. Chen, Y. Hu, S. Meng and X. Fu, *Appl. Catal., B*, 2014, **150–151**, 564–573.